

RbFe²⁺Fe³⁺F₆: Synthesis, Structure, and Characterization of a New Charge-Ordered Magnetically Frustrated Pyrochlore-Related Mixed-Metal Fluoride

Sun Woo Kim,^a Sang-Hwan Kim,^a P. Shiv Halasyamani,^{a,*} Mark A. Green,^b Kanwal Preet Bhatti,^c C. Leighton,^{c,*} Hena Das,^d and Craig J. Fennie^{d,*}

Received (in XXX, XXX) Xth XXXXXXXXXX 20XX, Accepted Xth XXXXXXXXXX 20XX
DOI: 10.1039/b000000x

A new charge-ordered magnetically frustrated mixed-metal fluoride with a pyrochlore-related structure has been synthesized and characterized. The material, RbFe₂F₆ (RbFe²⁺Fe³⁺F₆) was synthesized through mild hydrothermal conditions. The material exhibits a three-dimensional pyrochlore-related structure consisting of corner-shared Fe²⁺F₆ and Fe³⁺F₆ octahedra. In addition to single crystal diffraction data, neutron powder diffraction and magnetometry measurements were carried out. Magnetic data clearly reveal strong antiferromagnetic interactions (a Curie-Weiss temperature of -270 K) but sufficient frustration to prevent ordering until 16 K. No structural phase transformation is detected from the variable temperature neutron diffraction data. Infrared, UV-vis, thermogravimetric, and differential thermal analysis measurements were also performed. First-principles density functional theory (DFT) electronic structure calculations were also done. Crystal data: RbFe₂F₆, orthorhombic, space group Pnma (No. 62), a = 7.0177(6) Å, b = 7.4499(6) Å, c = 10.1765(8) Å, V = 532.04(8) Å³, Z = 4.

Introduction.

Mixed-metal fluorides are of topical interest attributable to their varied functional properties.¹ These include multiferroic behavior (BaNiF₄²⁻⁵ and Pb₅Cr₃F₁₉⁶), magnetic frustration, (Na₂NiFeF₇⁷ and MnCrF₅⁸), ferroelectricity, (K₃Fe₅F₁₅⁹⁻¹⁰ and SrAlF₅¹¹), and non-linear optical behavior (BaMgF₄).¹²⁻¹³ Recently, attention has been paid to the multiferroic K₃Fe₅F₁₅ and related materials such as K₃Cu₃Fe₂F₁₅ and K₃Cr₂Fe₂F₁₅,¹⁴⁻¹⁶ as well as multiferroic fluorides as a whole.¹⁷⁻¹⁸ K₃Fe₅F₁₅ and K₃Cu₃Fe₂F₁₅ have been shown to be ferri- and anti-ferromagnetic respectively, whereas K₃Cr₂Fe₂F₁₅ exhibits relaxor-like magnetic transitions. Although full structural data is lacking for the quaternary phases, multiferroic behavior is suggested.¹⁵⁻¹⁶ It should also be noted that in K₃Cu₃Fe₂F₁₅ and K₃Cr₂Fe₂F₁₅, the Cu²⁺ / Fe³⁺ and Cr³⁺ / Fe²⁺ cations respectively are crystallographically disordered.

With respect to AM²⁺M³⁺F₆ materials (A = alkali metal or NH₄; M²⁺ = Mg, Mn, Fe, Co, Ni, Cu; M³⁺ = Al, Ga, V, Cr, Fe) a host of materials have been reported,¹⁹⁻²⁰ although well-determined

crystal structures are lacking for many. Structure types for the AM²⁺M³⁺F₆ materials include trirutile (LiM²⁺M³⁺F₆),²¹ modified pyrochlore ((NH₄)Fe²⁺Fe³⁺F₆),²² tetragonal (K_{0.6}Fe²⁺_{0.6}Fe³⁺_{0.4}F₃),²³⁻²⁵ and hexagonal (K_{0.6}Nb₂F₆)²⁶ bronzes, and materials iso-structural to trigonal Na₂SiF₆ (LiMnGaF₆).²⁷ In these materials, both disorder and order are observed between the M²⁺ and M³⁺ cations. With the pyrochlore related materials, crystallographic disorder, of the M²⁺ and M³⁺ cations on the octahedral sites is observed. This disorder results in spin-glass behavior in CsMnFeF₆.²⁸⁻²⁹ Ordering of the M²⁺ and M³⁺ cations has been observed, with a lowering of crystallographic symmetry, in the trirutile LiFe²⁺Fe³⁺F₆,²¹ the fluorobronze K_{0.6}Fe²⁺_{0.6}Fe³⁺_{0.4}F₃,²³⁻²⁵ and the pyrochlore-related (NH₄)Fe²⁺Fe³⁺F₆.²² Antiferromagnetic behavior has been observed with the Li⁺ and NH₄ phases.^{21, 30} In addition to the aforementioned magnetic behavior, magnetic frustration has been observed in a variety of mixed-metal fluorides.¹ Such frustration can occur not only when the two metal cationic species, M²⁺ and M³⁺, crystallographically order, but also if they are arranged in some form of triangular structural topology, i.e. in the presence of geometric frustration. Magnetically frustrated fluorides include the hexagonal tungsten bronze – FeF₃,³¹ Na₂NiFeF₇,⁷ MnCrF₅,⁸ Fe₃F₈ · 2H₂O,³²⁻³³ and NH₄Fe₂F₆.³⁰

In this paper, we report on the synthesis, structure (X-ray and variable temperature neutron diffraction), and characterization of RbFe₂F₆ (RbFe²⁺Fe³⁺F₆). This new material represents an example of a charge-ordered pyrochlore-related mixed-metal fluoride that exhibits strong magnetic frustration. In addition to the synthesis and structural characterization, magnetic measurements and theoretical calculations are performed. These measurements and calculations enable us to develop and understand a variety of important structure-property relationships.

Experimental Section

Reagents. RbF (Alfa Aesar, 99.7%), FeF₂ (Alfa Aesar, 99%), FeF₃ (Alfa Aesar, 97%), and CF₃COOH (Alfa Aesar, 99%) were used without further purification.

Synthesis. RbFe₂F₆ was obtained by hydrothermal methods using a diluted CF₃COOH solution. 0.119 g (1.14×10⁻³ mol) of RbF, 0.107 g (1.14×10⁻³ mol) of FeF₂, 0.129 g (1.14×10⁻³ mol) of FeF₃, 3 ml (3.90×10⁻² mol) of CF₃COOH, and 5 ml of H₂O were combined in a 23-mL Teflon-lined stainless steel autoclave. The autoclave was closed, gradually heated to 230 °C, held for 24 h, and cooled slowly to room temperature at a rate 6 °C h⁻¹. The mother liquor was decanted, and the only solid product from the reaction, brown colored rod shaped crystals, subsequently shown to be RbFe₂F₆, was recovered by filtration and washed with distilled water and acetone. The yield was ~40 % based on FeF₃. Powder X-ray diffraction patterns on the synthesized phase are in good agreement with the generated pattern from the single-crystal data (see Figure S1).

Single Crystal X-ray Diffraction. A brown colored rod shaped crystal (0.02 x 0.02 x 0.1 mm³) was selected for single-crystal data collection. The data were collected using a Siemens SMART APEX diffractometer equipped with 1K CCD area detector using

graphite-monochromated Mo-K α radiation. A hemisphere of data was collected using a narrow-frame method with scan widths of 0.30° in ω and an exposure time of 45 s per frame. The data were integrated using the Siemens SAINT program,³⁴ with the intensities corrected for Lorentz, polarization, air absorption, and absorption attributable to the variation in the path length through the detector face plate. Psi-scans were used for the absorption correction on the data. The data were solved and refined using SHELXS-97 and SHELXL-97,³⁵⁻³⁶ respectively. All of the atoms were refined with anisotropic thermal parameters and the refinement converged for $I > 2\sigma(I)$. All calculations were performed using the WinGX-98 crystallographic software package.³⁷ Relevant crystallographic data, atomic coordinates and thermal parameters, and selected bond distance for RbFe₂F₆ are given in Tables 1, 2, and 3.

Table 1. Crystallographic Data for RbFe₂F₆

Parameter	RbFe ₂ F ₆
Formula Weight, fw	311.17
T (K)	296.0(2)
λ (Å)	0.71073
Crystal System	Orthorhombic
Space Group	<i>Pnma</i> (No.62)
a (Å)	7.0177(6)
b (Å)	7.4499(6)
c (Å)	10.1765(8)
V (Å ³)	532.04(8)
Z	4
ρ_{calcd} (g/cm ³)	3.885
μ (mm ⁻¹)	14.577
$2\theta_{\text{max}}$ (deg)	58.04
R (int)	0.0361
GOF	1.087
$R(F)^a$	0.0214
$R_w(F_o^2)^b$	0.0497

$$^a R(F) = \frac{\sum ||F_o| - |F_c||}{\sum |F_o|}, \quad ^b R_w(F_o^2) = \frac{[\sum w(F_o^2 - F_c^2)^2 / \sum w(F_o^2)^2]^{1/2}}$$

Table 2. Atomic Coordinates for RbFe₂F₆

Atom	x	Y
Rb(1)	0.9920(1)	0.25
Fe(1) (Fe ²⁺)	0.7967(1)	0.25
Fe(2) (Fe ³⁺)	0.5	0
F(1)	0.7364(2)	0.0633(2)
F(2)	0.3737(2)	0.0104(2)
F(3)	0.4359(3)	0.25
F(4)	0.5642(3)	0.25

^a U_{eq} is defined as one-third of the trace of the orthogonal U_{ij} tensor.

Table 3. Selected Bond Distances for RbFe₂F₆

Bond	Distance (Å)	Bond
Rb(1) — F(1)	3.042(1) × 2	Fe(1) — F(1)
Rb(1) — F(1)	3.071(1) × 2	Fe(1) — F(2)
Rb(1) — F(2)	3.050(2) × 2	Fe(1) — F(4)
Rb(1) — F(2)	3.248(1) × 2	Fe(1) — F(4)
Rb(1) — F(3)	3.239(2)	Fe(2) — F(1)
Rb(1) — F(4)	2.931(2)	Fe(2) — F(2)
		Fe(2) — F(3)

Powder X-ray Diffraction. The PXRD data of RbFe₂F₆ were collected on a PANalytical X'pert pro diffractometer using Cu K α radiation in the 2θ range 5-90°. A step size of 0.008 degrees (deg) with a scan time of 0.3 s/deg was used. No impurity phases were observed, and the calculated and experimental PXRD patterns are in good agreement (see Figure S1).

Neutron Diffraction. Powder neutron diffraction was performed on the BT1 high resolution diffractometer at the NIST Center for Neutron research. Data were collected using a Ge (311) monochromator at $\lambda = 2.0782$ Å and a (311) monochromator at $\lambda = 1.5401$ Å, with an in-pile collimation of 15°. Rietveld refinements were performed using the FULLPROF suite of programs.³⁸ Cooling was performed with a closed cycle refrigerator and measurements were performed at 4, 10, 25, 50, 100, 150, 200, 250 and 300 K.

Infrared Spectroscopy. Infrared spectra were collected on a Mattson FT-IR 5000 spectrometer in the 400 – 4000 cm⁻¹ range (see Figure S3).

UV-Vis Diffuse Reflectance Spectroscopy. UV-Vis diffuse reflectance spectra were collected on a Varian Cary 500 UV-Vis-NIR spectrophotometer from 200-1500 nm at room temperature. Poly-(tetrafluoroethylene) was used as a reference. Reflectance spectra were converted to absorbance using the Kubelka-Munk function (see Figure S4).³⁹⁻⁴⁰

Thermal Analysis. Thermogravimetric analysis was carried out on a EXSTAR TG/DTA 6300 (SII NanoTechnology Inc.). About 10 mg of the sample was placed into a platinum crucible and heated under a nitrogen atmosphere at a rate of 10 °C min⁻¹ to 1000 °C (see Figure S5).

Magnetic Measurements. DC magnetometry measurements were performed in helium gas in a commercial SQUID (Superconducting Quantum Interference Device) magnetometer (Quantum Design) at temperatures from 4.0 to 300 K, in applied magnetic fields up to 70 kOe. For low field measurements the remnant field in the superconducting magnet was nulled using a compensating coil in unison with a fluxgate.

Theoretical Calculations. First-principles electronic structure calculations based on density functional theory (DFT) were performed using the Perdew-Burke-Ernzerhof (PBE)⁴¹ form of exchange correlation functional under the generalized gradient approximation (GGA). The projected augmented plane wave (PAW)⁴² method was employed as implemented in the Vienna Ab-initio Simulation Package (VASP).⁴³⁻⁴⁴ The valence electron configurations used in the present study are follows: 4p⁶5s¹ for Rb, 3p⁶3d⁷4s¹ for Fe and 2s²2p⁵ for F. We used a 500 eV plane wave cutoff to generate the basis set, and a 4×4×2 Monkhorst-Pack k-point mesh to sample the electronic Brillouin zone. The optimization of the internal structural parameters were carried out and optimized until the forces on each atom of the system become < 0.001 eV/Å. Within density-functional theory, the failure of the generalized gradient approximation (GGA) to properly capture the physics of correlated systems is well established. A widely accepted approach beyond GGA is the GGA plus Hubbard U (GGA+U) method.⁴⁵ We employed the rotationally invariant scheme proposed by Dudarev et al.⁴⁶ in which a single parameter is $U_{eff} = U - JH$, where U and JH represent the effective on-site screened Coulomb and exchange interaction is introduced on the Fe-atom. The structural, electronic and magnetic properties of RbFe₂F₆ have been investigated both in GGA and in GGA+U for the range of U_{eff} equal to 1.0 to 7.0 eV. Qualitatively, all results remain insensitive to $U_{eff} > 4.0$ eV therefore we present results for GGA and GGA+U = 6eV (See supplemental for entire complete study, from it a high level of confidence is obtained that a suitable value of the on-site Coulomb interaction lies between 6.0 to 7.0 eV. Such fine-tuning of U does not alter the physics discussed here.)

Results

Structure. RbFe₂F₆ crystallizes in the Pnma space group with lattice parameters of a = 7.02134(7) Å, b = 7.45093(7) Å and c = 10.1795(1) Å at room temperature. This represents a reduced orthorhombic cell of the conventional β-pyrochlore lattice with the Fd-3m symmetry. The β-pyrochlore is related to the more common α-pyrochlore lattice, with the general formula A₂B₂X₆X', through two ordered vacancies. Firstly, one of the two A cations is vacant, which reverts the Kagome network of the A sites in α-pyrochlore into a diamond lattice with T_d point symmetry. Secondly, the anion, X', that does not contribute to the

BX₆ octahedra is vacant; removing this apical anion reduces the eight-coordination of the A cation and leaves an open cage site.

RbFe₂F₆ exhibits a three-dimensional crystal structure consisting of corner-shared FeF₆ octahedra that are separated by Rb⁺ cations (see Figures 1 and 2). The formula may be more descriptively written as RbFe²⁺Fe³⁺F₆, as the Fe²⁺ and Fe³⁺ cations are ordered in the structure. The structure of RbFe₂F₆ may be described as being built up from two connected FeF₆ octahedral sub-lattices. Polyhedral and ball-and-stick representations of RbFe₂F₆ are shown in Figures 1 and 2. The bc-plane of the structure is shown in Figure 1, and as can be seen chains of Fe³⁺F₆ octahedra share corners along the b-axis direction. These Fe³⁺F₆ chains are connected through Fe²⁺F₆ octahedra along the c-axis direction. The ac-plane of the structure is shown in Figure 2. Similarly,

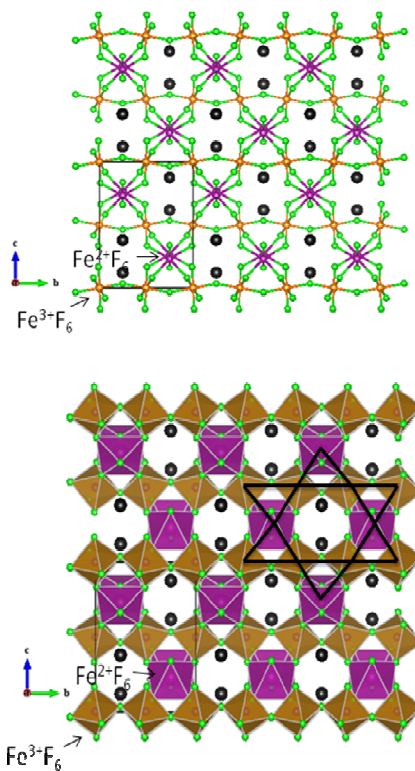


Figure 1. Ball-and-stick (top) and polyhedral (bottom) representations of RbFe₂F₆ in the bc-plane. Note the Kagome-type nets in the bottom figure (dark lines).

chains of Fe²⁺F₆ octahedra share corners along the a-axis direction, and these chains are connected through Fe³⁺F₆ octahedra along the c-axis direction. This octahedral connectivity results in Kagome-type nets in both the bc- and ac-planes of the structure (see Figures 1b and 2b). The Fe²⁺ - F (Fe³⁺ - F) bond distances range between 1.961(2)-2.1368(13)Å (1.9098(14)-1.9488(6)Å). The Rb⁺ cation is in a 10-fold coordinated environment, with Rb-F distances that range between 2.931(2)-3.2477(14) Å. In connectivity terms, the structure may be written as {(Fe(II)F_{6/2})⁻ (Fe(III)F_{6/2})⁰]⁻ where charge balance is maintained by a Rb⁺ cation. Bond valence calculations⁴⁷⁻⁴⁸ (see Table 4) result in values of 0.821, 1.93, 3.03 and 0.935-0.996 for

Rb⁺, Fe²⁺, Fe³⁺ and F⁻ respectively.

Table 4. Bond valence analysis for RbFe₂F₆^a

Atom	F(1)	F(2)	F(3)	F(4)	Σ _{cations}
Rb(1)	0.092 ^[x2] 0.085 ^[x2]	0.090 ^[x2] 0.053 ^[x2]	0.054	0.124	0.818
Fe(1)	0.288 ^[x2]	0.268 ^[x2]	-	0.431 0.380	1.92
Fe(2)	0.533 ^[x2]	0.536 ^[x2]	^[x2] 0.482 ^[x2]	-	3.10
Σ _{anions}	0.998	0.947	1.02	0.935	

^a Bond Valence sums calculated with the formula: $S_i = \exp[(R_0 - R_i)/B]$, where S_i is a valence of the bond “ i ”, R_0 is a constant dependent upon the bonded elements, R_i is the bond length of bond i and B equals 0.37. Left and right superscripts indicate the number of equivalent F bonds for anions and cations, respectively.

10

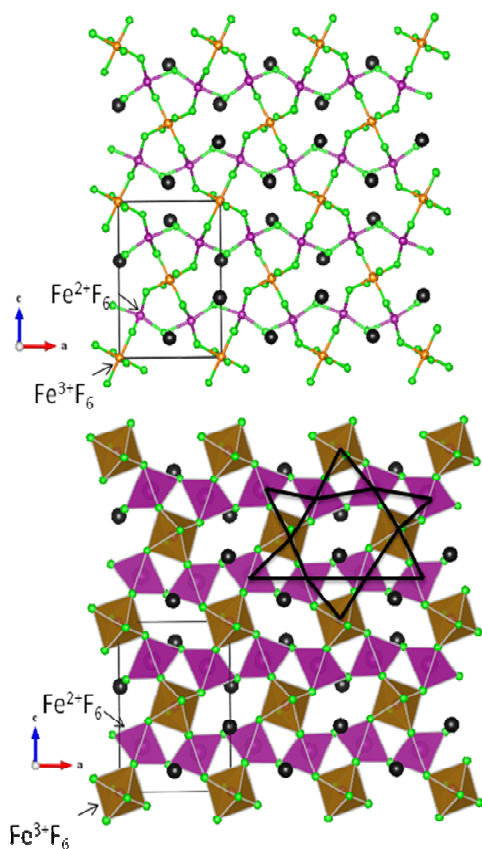


Figure 2. Ball-and-stick (top) and polyhedral (bottom) representations of RbFe₂F₆ in the ac-plane. Note the Kagome-type nets in the bottom figure (dark lines).

15

Neutron Diffraction. Powder neutron diffraction measurements were performed on RbFe₂F₆ at several temperatures in the range 4 - 300 K. Figure 3 shows the typical quality of fit to the observed data with this model, as obtained at 300 K, resulting in goodness-of-fit factors of $wRp = 4.49$ and $\chi^2 = 1.29$. One key feature of β -pyrochlores that has generally hindered their usefulness as model

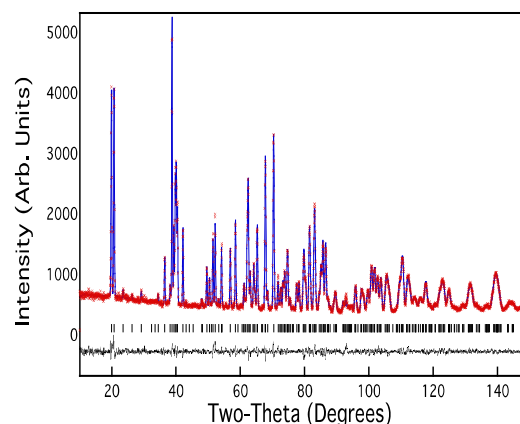


Figure 3. Observed (red), calculated (blue) and difference (black) data obtained from Rietveld refinements of neutron diffraction data of RbFe₂F₆ at 300 K.

magnetic systems is their tendency for both site disorder and partial occupancy. To evaluate these possibilities a number of models were tested and no evidence could be found for such issues in RbFe₂F₆; varying the occupancy of Rb from the ideal value of 1.0 gave a refined value of 0.99(1) and, as this made no improvement to the goodness-of-fit factors, this parameter was fixed in all subsequent refinements.

Infrared Spectroscopy. The FT-IR spectra of RbFe₂F₆ revealed Fe-F vibrations between 1000 and 400 cm⁻¹. The bands occurring between 750 – 700 cm⁻¹ and 530 – 400 cm⁻¹ can be assigned to Fe – F and Fe – F – Fe vibrations, respectively. These assignments are consistent with previous reports.⁴⁹ The IR spectra and assignments have been deposited in the supporting information (see Figure S3).

UV-Vis Diffuse Reflectance Spectroscopy. The UV-vis diffuse reflectance spectra indicate that the absorption energy for RbFe₂F₆ is approximately 1.9eV, consistent with the brown color of the material. Absorption (K/S) data were calculated through the Kubelka-Munk function:

$$F(R) = (1 - R)^2 / 2R = K/S$$

45

where R represents the reflectance, K the absorption, and S the scattering. In a K/S versus $E(eV)$ plot, extrapolating the linear part of rising curve to zero provides the onset of absorption at 1.9 eV. One of three bands in the region of 1.5 – 3.3 eV were attributed to d-d transitions of Fe, the other large broad bands in the region of 3.5 – 5.0 eV were attributed to metal to ligand charge transfer. The UV-vis diffuse reflectance spectra have been deposited in the supporting information (see Figure S4).

Thermal Analysis. The thermal behavior of RbFe₂F₆ was investigated using thermogravimetric analysis (TGA) and differential thermal analysis (DTA) under a N₂ atmosphere. The decomposition started around 350 °C and an additional step was also observed at around 600 °C, which is likely attributable to the

loss of fluorides. The DTA also showed two endothermic peaks at ~ 450 °C and ~ 750 °C, that indicate decomposition. Thermogravimetric analysis and differential thermal analysis diagrams for RbFe_2F_6 have been deposited in the supporting information, Figure S5. The final residue products, RbFeF_3 and FeF_2 , were confirmed by PXRD (see Figure S6).

Magnetic Measurements. Figure 4 shows a summary of the basic magnetic characterization of a powder sample of RbFe_2F_6 . The data shown are measured in an applied magnetic field (H) of 1 kOe, after field cooling (FC) and zero field cooling (ZFC). As shown in panel (a) the d.c. magnetic susceptibility (χ) is positive, exhibiting a monotonic increase with decreasing temperature down to 16 ± 0.5 K, at which point a prominent peak occurs (see inset) and the FC and ZFC curves bifurcate. The $\chi(T)$ behavior is thus typical of an antiferromagnet, consistent with the low T neutron diffraction analysis discussed below.

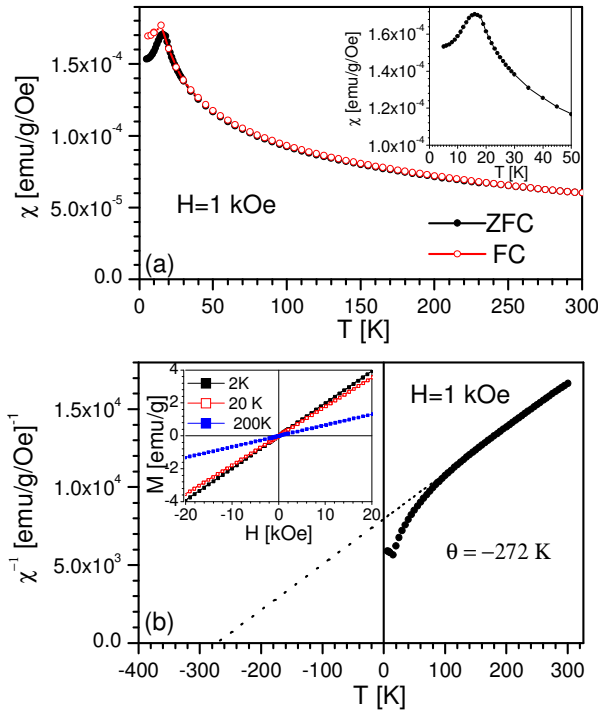


Figure 4. Temperature dependence of (a) the d.c. magnetic susceptibility measured in 1 kOe (after zero field and field cooling), and (b) the inverse magnetic susceptibility with a Curie-Weiss fit (dotted line). The extracted parameters are shown in the figure. The inset to (a) shows a close up of the low temperature region revealing the 16 K Néel temperature. The inset to (b) shows the linear magnetization vs. field behavior over the whole temperature range studied.

Theoretical Calculations. We optimized the internal structural degrees of freedom keeping the lattice parameters fixed at their experimental values at 4 K. The results using both spin-polarized GGA and GGA+U method with $U_{\text{eff}} = 4.0$ eV are listed in Table 5, together with the neutron diffraction data. (Note that the internal structural parameters remain constant for $U_{\text{eff}} > 4.0$ eV.) Both GGA and GGA+U results are in excellent agreement with the neutron diffraction data with the GGA+U method showing a slight improvement.

35

Table 5. Internal structural parameters optimized with spin polarized GGA and GGA+U methods with $U_{\text{eff}} = 4.0$ eV, together with the neutron powder diffraction data at 4 K refined with Rietveld method. Only the free parameters are listed. The differences between the internal structural parameters optimized using first principles DFT based methods and determined by neutron powder diffraction are given within parentheses.

Atom	Parameters	GGA	GGA+U ($U_{\text{eff}} = 4.0$ eV)	Experiment
Rb	x	0.993 (0.002)	0.990 (0.005)	0.995
	z	0.372 (0.007)	0.376 (0.003)	0.379
Fe(1)	x	0.808 (-0.007)	0.804 (-0.003)	0.801
	z	0.729 (0.001)	0.730 (0.000)	0.730
F(1)	x	0.748 (-0.007)	0.746 (-0.005)	0.741
	y	0.073 (-0.009)	0.066 (-0.002)	0.064
F(2)	z	0.578 (0.000)	0.576 (0.002)	0.578
	x	0.372 (0.007)	0.380 (-0.001)	0.379
F(3)	y	0.018 (-0.010)	0.007 (0.001)	0.008
	z	0.678 (-0.009)	0.673 (-0.004)	0.669
F(4)	x	0.425 (0.008)	0.422 (0.011)	0.433
	z	0.451 (0.017)	0.464 (0.004)	0.468
	x	0.576 (-0.007)	0.574 (-0.005)	0.569
	z	0.843 (-0.002)	0.844 (-0.003)	0.841

To elucidate the electronic structure of the system we have calculated and analyzed the partial density of states (PDOS) projected onto the 3d states of the two inequivalent iron ions, Fe(1) and F(2), and onto the F - 2p states. These states are situated near the Fermi energy and are therefore expected to dominate the electronic and magnetic properties of the system. The PDOS are computed for the lowest energy collinear spin configuration – a partially frustrated antiferromagnetic configuration (see Discussion for details) – within GGA and GGA+U. As typically found for magnetic oxides/fluorides, GGA leads to a half metallic solution in which there is a gap at the Fermi level in the spin-up channel while the spin-down channel is metallic. The 3d states of both Fe(1) and Fe(2), with significant admix with F-2p states, show complete occupancy in the up spin channel (see Figure 5a). On the other hand in the spin-down channel the 3d states of both Fe(1) and Fe(2) are partially filled. In order to show this change in occupancy of Fe-3d states in the down spin channel more clearly, we show in Figures 5c and 5e the Fe-3d PDOS and the integrated PDOS, respectively, plotted for a narrow energy window (-0.5 eV to 1.0 eV) around the Fermi level. As can be seen, Fe(1) d-states are slightly more occupied compared to Fe(2). This results in a slight charge disproportionation between Fe(1) and Fe(2), which is also reflected in the calculated magnetic moments of magnitude $3.83 \mu_{\text{B}}$ and $3.97 \mu_{\text{B}}$ at the Fe(1) and Fe(2) site respectively.

70

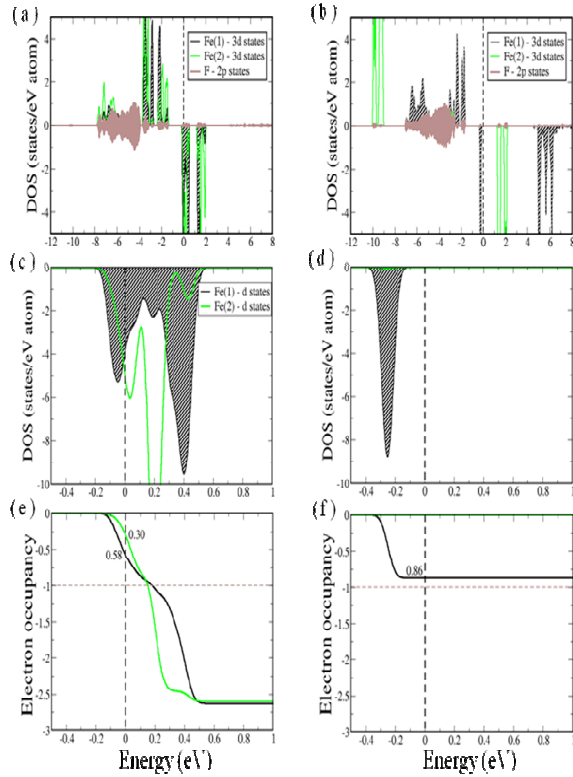


Figure 5. Upper panel and middle panel represent the partial density of states (PDOS) projected on to Fe(1)-3d (shaded with black diagonal lines), Fe(2)-3d (green solid line) and F-2p (brown shaded region) states computed with GGA (a & c) and GGA+U (b & d) methods for $U_{eff} = 6.0$ eV, plotted for a large energy window of range -12.0 eV to 8.0 eV and for a small energy window around Fermi energy of range -0.5 eV to 1.0 eV, respectively. Third panel corresponds to the integrated DOS (IDOS) in the down-spin channel of Fe(1)-3d PDOS (black solid line) and Fe(2)-3d PDOS (green solid line). The black dashed vertical line corresponds to Fermi level and the brown horizontal line shows the occupancy = 1.0.

Within GGA+U ($U_{eff} = 6$ eV) the band gap of $RbFe_2F_6$ opens. The calculated value of $E_{gap} = 1.3$ eV is slightly underestimated from the measured optical band gap of 1.9 eV determined from UV-vis diffuse spectra. As shown in Figure 5b, the 3d states of both Fe(1) and Fe(2) also remain completely occupied in the up spin channel. The modification of the occupancy of the 3d states of Fe ions, however, is found to be significant in the down spin channel. (This remains true throughout the entire range of $U_{eff} = 1.0$ to 7.0 eV as shown in the Supporting Information.) In Figure 5d and 5f we show the Fe-3d PDOS and the integrated PDOS, respectively, plotted for a narrow energy window (-0.5 eV to 1.0 eV) around the Fermi level. With the increase of the on-site Coulomb interaction (U) a 3d state of Fe(1) is found to move towards the valence region and is completely occupied. The calculated occupancy of Fe(1)-3d states in the down spin channel is found to be 0.86 (for all $U_{eff} \geq 4.0$ eV), which is reduced from 1.00 attributable to hybridization with F-2p states. This is consistent with a nominal oxidation state of Fe(1) being +2 and hence a d^6 electronic configuration. Whereas the completely empty spin-down channel for Fe(2) 3d states leads to the nominal valence of +3 and the d^5 electronic configuration. We therefore have an Fe^{+2}/Fe^{+3} charge ordered ground state and an energy

gap of the system that is between the 3d states of Fe(1) and Fe(2), which is in agreement with the nature of the optical gap obtained from UV-vis diffuse spectra. The charge separation between Fe(1) and Fe(2) is also reflected in the computed magnetic moments of $3.82 \mu_B$ and $4.48 \mu_B$ at Fe(1) and Fe(2) site respectively. Further strong evidence of a charge ordered ground state is found from a plot of the charge density within a small energy window below the Fermi energy (-0.5 eV to 0.0 eV), within GGA and GGA+U as shown in Figures 6a and 6b respectively. Within GGA+U it can clearly be seen that an extra electron occupies an Fe(1) state in the spin-down channel compared with Fe(2).

Discussion.

Synthesis. Previously reported and related materials, e.g., $NH_4Fe_2F_6$, NH_4MnFeF_6 , NH_4MnCrF_6 , and $RbMnFeF_6$,^{22, 50} were synthesized by using the binary metal fluorides mixed with the alkali metal fluoride of NH_4F solutions in a platinum tube. The tube was sealed, placed in an autoclave, and heated to temperatures above 350°C that resulted in pressures in excess of 2000 bar. We were able to synthesize $RbFe_2F_6$ through a low temperature and mild hydrothermal technique. In our method, the binary metal fluorides are combined with RbF and a diluted CF_3COOH aqueous solution. We have previously demonstrated that this method can be used to synthesize phase-pure and polycrystalline $BaMF_4$ ($M = Mg, Mn, Co, Ni$ and Zn).⁵¹

Variable Temperature Neutron Diffraction Data. Figure 7 shows the lattice parameters from the variable temperature neutron diffraction data. All three lattice parameters show a modest contraction down to the magnetic ordering temperature, below which there is negative thermal expansion, particularly within the ab -plane. This is confirmed through the increase in volume, as shown in the inset to Figure 7b. No structural phase transition was found on cooling, and $RbFe_2F_6$ remained

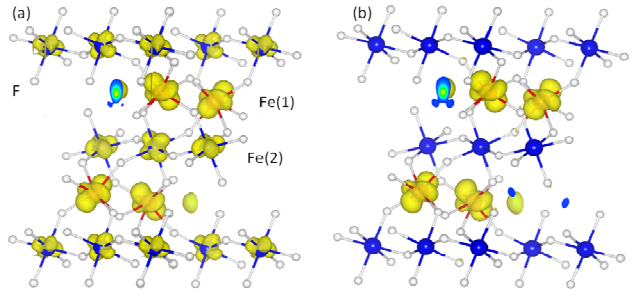


Figure 6. The electron charge density plotted for the energy range of -0.5 eV below the Fermi level, computed with GGA (a) and GGA+U (b) methods with $U_{eff} = 6.0$ eV. The isovalue is set to $0.05 e/\text{\AA}^3$.

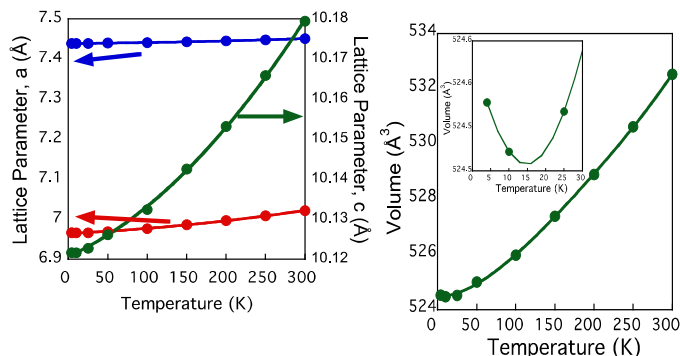


Figure 7. Panel a shows the lattice parameter as a function temperature; there is a contraction in all three directions upon cooling, until the magnetic ordering temperature when RbFe_2F_6 shows negative thermal expansion in a, b and c best visualized by panel b the overall increase in volume.

orthorhombic with $Pnma$ symmetry to the lowest temperature measured. One central structural feature was the difference between thermal factors of the constituent elements. Figure 8 shows the isotropic thermal factor for all 6 atoms as a function of temperature. Although each atom has a typical temperature dependence, the absolute value of U for Rb is ≈ 5 times that of

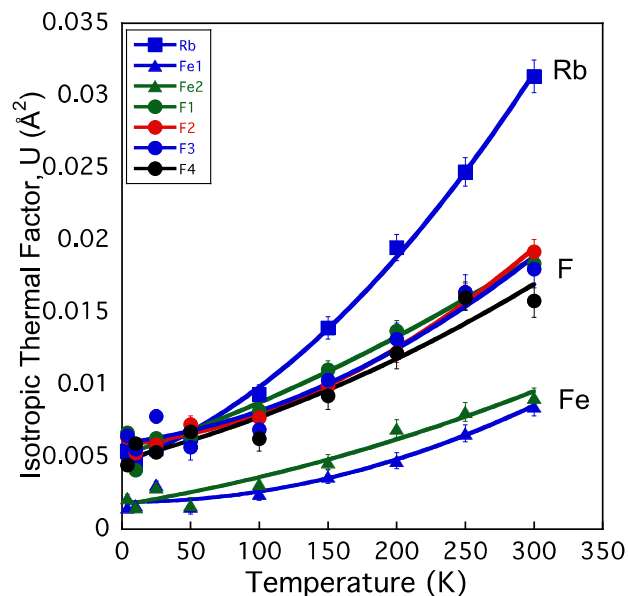


Figure 8. Isotropic thermal factors of RbFe_2F_6 as a function of temperature as obtained from Rietveld refinement of powder neutron diffraction data showing the extraordinary large thermal factor of Rb as a result of the mismatch between Rb ionic size and the open cage site that it occupied.

the lighter Fe, and even twice that of the F that is over four times lighter. The rattling effect of A site cations within the β -pyrochlores is well documented and results from a gross mismatch between the ionic radii of the cations and the available space. The magnetic structure was determined from powder neutron diffraction data collected at 4 K on the BT1

diffractometer at NIST. The new magnetic reflections that appeared below T_N could all be indexed with a $k = (0\ 0\ 0)$ propagation vector. Representational analysis in the $Pnma$ space group, calculated with the BASIREPS program, showed eight possible irreducible representations for the two iron atoms at Fe(1) ($x\ 0.25\ z$) and Fe(2) ($0.5\ 0\ 0.5$). Each possibility was evaluated in the FULLPROF program³⁸ and a summary of the representations and comparison of the magnetic R-factors is given in Table 6.

Table 6. Irreducible representations of Fe(1) at ($x\ 0.5\ z$) and Fe(2) at ($0.5\ 0\ 0.5$) in the $Pnma$ space group and a ($0\ 0\ 0$) propagation vector are shown. A comparative magnetic R-factor before full refinement is given in the final column and represents the experimental determined magnetic structure.

Irrep Rep.	Atom Position	Basis Vector for Fe ($0.80\ 0.25\ 0.73$)	Basis Vector for Fe ($0.5\ 0\ 0.5$)	R_{mag}
Γ_1	(x, y, z) ($x+\frac{1}{2}, y, z+\frac{1}{2}$) ($x, y+\frac{1}{2}, z$) ($x+\frac{1}{2}, y+\frac{1}{2}, z+\frac{1}{2}$)	($0\ 1\ 0$) ($0\ -1\ 0$) ($0\ 1\ 0$) ($0\ -1\ 0$)	($1\ 0\ 0$) ($0\ 1\ 0$) ($0\ 0\ 1$) ($-1\ 0\ 0$) ($0\ -1\ 0$) ($0\ 0\ 1$) ($-1\ 0\ 0$) ($0\ 1\ 0$) ($0\ 0\ -1$) ($1\ 0\ 0$) ($0\ -1\ 0$) ($0\ 0\ 1$)	8.82
Γ_2	(x, y, z) ($x+\frac{1}{2}, y, z+\frac{1}{2}$) ($x, y+\frac{1}{2}, z$) ($x+\frac{1}{2}, y+\frac{1}{2}, z+\frac{1}{2}$)	($1\ 0\ 0$) ($0\ 0\ 1$) ($-1\ 0\ 0$) ($0\ 0\ 1$) ($1\ 0\ 0$) ($0\ 0\ -1$) ($1\ 0\ 0$) ($0\ 0\ -1$)		88.1
Γ_3	(x, y, z) ($x+\frac{1}{2}, y, z+\frac{1}{2}$) ($x, y+\frac{1}{2}, z$) ($x+\frac{1}{2}, y+\frac{1}{2}, z+\frac{1}{2}$)	($1\ 0\ 0$) ($0\ 0\ 1$) ($-1\ 0\ 0$) ($0\ 0\ 1$) ($1\ 0\ 0$) ($0\ 0\ 1$) ($-1\ 0\ 0$) ($0\ 0\ 1$)	($1\ 0\ 0$) ($0\ 1\ 0$) ($0\ 0\ 1$) ($-1\ 0\ 0$) ($0\ -1\ 0$) ($0\ 0\ 1$) ($1\ 0\ 0$) ($0\ -1\ 0$) ($0\ 0\ 1$) ($-1\ 0\ 0$) ($0\ 1\ 0$) ($0\ 0\ 1$)	13.1
Γ_4	(x, y, z) ($x+\frac{1}{2}, y, z+\frac{1}{2}$) ($x, y+\frac{1}{2}, z$) ($x+\frac{1}{2}, y+\frac{1}{2}, z+\frac{1}{2}$)	($0\ 1\ 0$) ($0\ -1\ 0$) ($0\ -1\ 0$) ($0\ 1\ 0$)		104
Γ_5	(x, y, z) ($x+\frac{1}{2}, y, z+\frac{1}{2}$) ($x, y+\frac{1}{2}, z$) ($x+\frac{1}{2}, y+\frac{1}{2}, z+\frac{1}{2}$)	($0\ 1\ 0$) ($0\ 1\ 0$) ($0\ 1\ 0$) ($0\ 1\ 0$)	($1\ 0\ 0$) ($0\ 1\ 0$) ($0\ 0\ 1$) ($1\ 0\ 0$) ($0\ 1\ 0$) ($0\ 0\ -1$) ($-1\ 0\ 0$) ($0\ 1\ 0$) ($0\ 0\ -1$) ($-1\ 0\ 0$) ($0\ 1\ 0$) ($0\ 0\ 1$)	19.3
Γ_6	(x, y, z) ($x+\frac{1}{2}, y, z+\frac{1}{2}$) ($x, y+\frac{1}{2}, z$) ($x+\frac{1}{2}, y+\frac{1}{2}, z+\frac{1}{2}$)	($1\ 0\ 0$) ($0\ 0\ 1$) ($1\ 0\ 0$) ($0\ 0\ -1$) ($-1\ 0\ 0$) ($0\ 0\ -1$) ($-1\ 0\ 0$) ($0\ 0\ 1$)		88
Γ_7	(x, y, z) ($x+\frac{1}{2}, y, z+\frac{1}{2}$) ($x, y+\frac{1}{2}, z$) ($x+\frac{1}{2}, y+\frac{1}{2}, z+\frac{1}{2}$)	($1\ 0\ 0$) ($0\ 0\ 1$) ($1\ 0\ 0$) ($0\ 0\ -1$) ($1\ 0\ 0$) ($0\ 0\ 1$) ($1\ 0\ 0$) ($0\ 0\ -1$)	($1\ 0\ 0$) ($0\ 1\ 0$) ($0\ 0\ 1$) ($1\ 0\ 0$) ($0\ 1\ 0$) ($0\ 0\ -1$) ($1\ 0\ 0$) ($0\ -1\ 0$) ($0\ 0\ 1$) ($1\ 0\ 0$) ($0\ -1\ 0$) ($0\ 0\ -1$)	20.8
Γ_8	(x, y, z) ($x+\frac{1}{2}, y, z+\frac{1}{2}$) ($x, y+\frac{1}{2}, z$) ($x+\frac{1}{2}, y+\frac{1}{2}, z+\frac{1}{2}$)	($0\ 1\ 0$) ($0\ 1\ 0$) ($0\ -1\ 0$) ($0\ -1\ 0$)		81.2

Γ_1 was clearly identifiable as giving the best fit to the experimental data. Within this representation, the moments of Fe at ($x\ 0.25\ z$) are confined to the b axis, whereas the second Fe position at ($0.5\ 0\ 0.5$) is allowed to have components along either the a , b or c axis. However, refinement of the moment on the

second Fe position only gave contributions along the a axis, and no improvement to the fit of the powder neutron diffraction data could be achieved with additional components along b or c . These latter components were omitted from the final refinements.

The atomic positions of the final refinements are given in Table 7

Atom	x	y	z	B	Moment
Rb	0.9942 (3)	0.25 (-)	0.3798 (2)	0.43 (3)	
Fe1	0.8014 (2)	0.25 (-)	0.7302 (1)	0.20 (2)	3.99 (5)
Fe2	0.5	0.0	0.5	0.17 (2)	4.29 (5)
F1	0.7413 (2)	0.0644 (2)	0.5784 (2)	0.53 (3)	
F2	0.3791 (2)	0.0077 (3)	0.6698 (1)	0.50 (3)	
F3	0.4322 (3)	0.25	0.4672 (2)	0.51 (4)	
F4	0.5682 (3)	0.25	0.8407 (2)	0.35 (3)	

Table 7. Refined atomic positions as obtained from Rietveld refinement of the powder neutron diffraction at 4 K in the Pnma space group with cell parameters of $a = 6.96630$ (5) Å, $b = 7.43903$ (5) and $c = 10.12164$ (7) Å. Final $wRp = 4.34$ %, $R_{Bragg} = 2.17$ % and a magnetic R-factor of 3.35%.

and the observed, calculated and difference plots are shown in Figure 9. The magnetic structure is shown in Figure 10. Fe(1) with a magnetic moment of $3.99(5) \mu_B$ is confined to the b axis, but can be described as forming antiferromagnetic chains along the a -axis. These chains are orthogonal to those on Fe(2). The second Fe moment at $(0.5 \ 0 \ 0.5)$ has a slightly larger magnitude of $4.29(5) \mu_B$, consistent with its Fe^{3+} oxidation state, and resides along the a -axis forming antiferromagnetic chains parallel to the b -axis. The refined moments are all smaller than the theoretical spin-only contribution to the magnetic moment, but this is consistent with the observed diffuse scattering that is present even at 4 K, resulting from the magnetic frustration, suggesting that not all of the moments become long-range ordered. The refined moments are, however, consistent with the GGA+U calculated moments, $Fe(1)_{calc(exp)} = 3.82\mu_B$ ($3.99(5)\mu_B$) and $Fe(2)_{calc(exp)} = 4.48\mu_B$ ($4.29(5)\mu_B$).

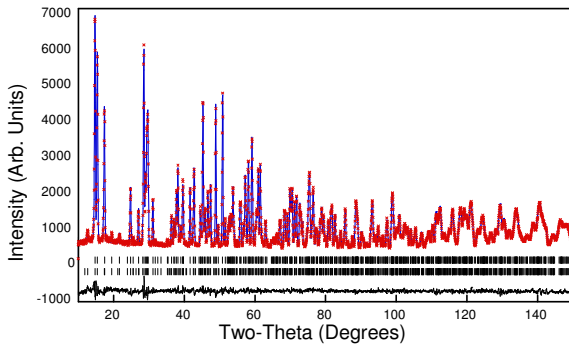


Figure 9. Observed (red), calculated (blue) and difference (black) data obtained from Rietveld refinements of neutron diffraction data of $RbFe_2F_6$ at 4 K. The upper tickmarks represent those associated with the nuclear structure while those below correspond to the magnetic structure refinement.

Magnetism. Considerable additional information can be gathered from the χ^{-1} vs. T plot shown in Figure 4b. The data are seen to adhere quite well to the Curie-Weiss (C-W) form ($\chi = C/T - \theta$), where C and θ are constants) for $T > 100$ K or so, yielding a Weiss temperature of -272 K. Fits with an additional temperature-independent paramagnetic susceptibility describe the data even better, yielding an effective number of Bohr magnetons of $7.9 \mu_B$ / f.u. Note that measurement of $\chi(T)$ in magnetic fields in the range $10-10^4$ Oe yielded magnetic moment and θ values that varied by only 10-20 %, consistent with the fact that the $M(H)$ curves are quite linear at all T (see inset to Figure 4b). The extracted values are similarly robust with respect to the exact temperature range used for the fitting to the C-W form. The theoretical spin only value is $7.7 \mu_B$ / f.u. ($Fe^{2+} = 4.9 \mu_B$, $Fe^{3+} = 5.9 \mu_B$), in good agreement with the data. Importantly, the large negative Weiss temperature indicates relatively strong AF interactions between the Fe moments. In fact, comparison to the actual AF ordering temperature of 16 K indicates significant magnetic frustration in this compound, with a frustration ratio (θ / T_N) of 17.⁵²

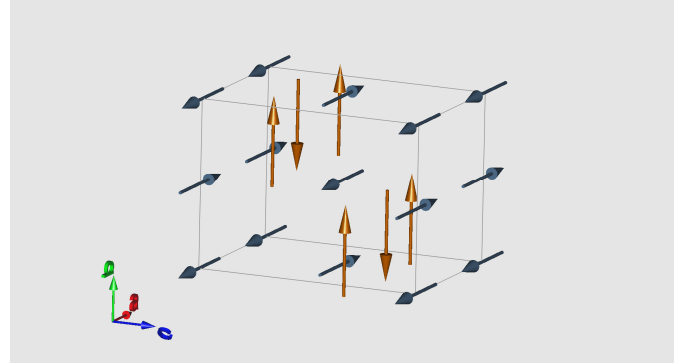


Figure 10. Magnetic structure of $RbFe_2F_6$ at 4 K as determined from Rietveld refinement of powder neutron diffraction data. The magnetic structure has a $(0 \ 0 \ 0)$ propagation vector with the Fe(1) moment (gold) aligned along the b axis forming antiferromagnetic chains down a , whereas the Fe(2) moments (blue) align along the a axis and form antiferromagnetic chains along b .

Theoretical Calculations. We elucidate the magnetic properties of $RbFe_2F_6$ by expanding the total energy of the system using the Heisenberg model,

$$E = E_0 - \sum_{ij} J_{ij} S_i \cdot S_j \quad (1)$$

where E_0 is the total energy of the system in the orthorhombic symmetry without spin-spin interaction. Here S_i is the spin of the i^{th} Fe ion and J_{ij} denotes the exchange integral between i^{th} and j^{th} Fe ions. A negative (positive) value of J corresponds to antiferromagnetic (ferromagnetic) nature of the coupling. The magnetic exchange integrals J can be found by fitting the total energy equations for eight collinear spin configurations assuming $S = 2$ and $S = 5/2$ for Fe(1) and Fe(2) ions respectively. We have considered all the nearest neighbor (NN) exchange integrals around each Fe ion. The exchange integral pathways that we

considered in the expansion of the total energy are given in Figure 11a. It is important to note that these paths construct an Fe_4 tetrahedral unit, which is the basic building block of the magnetic network of the system. Therefore the system is expected to be completely geometrically frustrated when all these NN interactions, J_1 to J_4 , are antiferromagnetic in nature and exactly

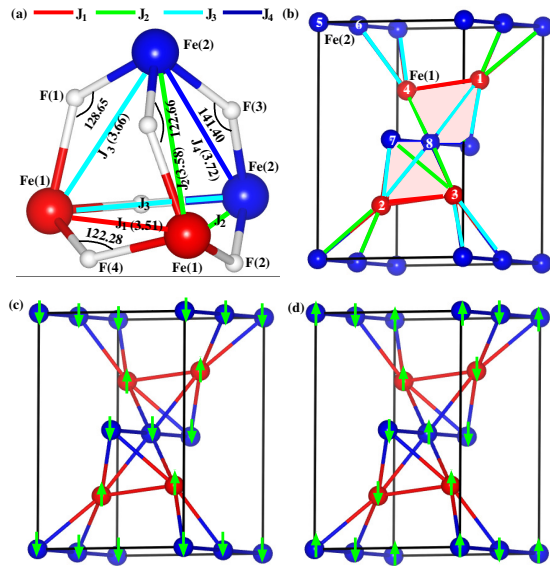


Figure 11. In the upper panel: (a) represents the Fe_4 tetrahedron and (b) represents the magnetic unit cell. The Fe-Fe distances are in Å given inside the parentheses. The pink shaded regions show the Fe_4 tetrahedron unit. Eight Fe ions in the orthorhombic unit cell have been numbered. In the lower panel: (c) and (d) show SC-2 and SC-4 respectively.

equal in magnitude to each other. The nature, as well as the magnitudes of these exchange integrals therefore plays a crucial role to drive the stability of the magnetic ground state of the system.

The total energy results for each of the eight spin configurations are described in Table 8 where we find in both GGA and GGA+U that the ground state is antiferromagnetic (AFM). The minimum collinear AFM spin configuration (SC) energy, however, is found to switch between two AFM configurations, SC-2 to SC-4, when we include finite correlation effects (we calculate the ground state to be SC-4 for all $U_{\text{eff}} > 1\text{eV}$). The main difference between these two states is the coupling within a chain of spins. For SC-2, the spins are coupled ferromagnetically along both the Fe(1) and the Fe(2) chains, with the coupling between chains being antiferromagnetic (see Figure 11c). In contrast to this, in SC-4, spins are antiferromagnetically coupled along both the Fe(1) and the Fe(2) chains, while the chains remain antiferromagnetically coupled to each other (see Figure 11d). SC-4 is close to the experimentally determined non-collinear spin structure (see Figure 10).

Table 8. Eight spin configurations of the Fe ions within the orthorhombic unit cell used to determine the lowest energy collinear spin configuration and the magnetic exchange integrals, J_1 to J_4 (as described in Figures 11a and b), where $E1 = -J_1 S_1 S_1$, $E2 = -J_2 S_1 S_2$, $E3 = -J_3 S_1 S_2$ and $E4 = -J_4 S_2 S_2$. S_1 and S_2 represent the spin of Fe(1) and Fe(2) respectively. + and - sign correspond to spin up and down respectively. Numbering of the magnetic ions follow Figure 11b. In the last two columns the calculated total energies of the collinear spin configurations obtained using GGA and GGA+U method with $U_{\text{eff}} = 6.0\text{eV}$ are given respectively, with respect to the spin configuration 1, where all spins are pointing along same direction.

Confg.	Magnetic ions								Total energy equations	Calculated total energy (meV)	
	1	2	3	4	5	6	7	8		GGA	GGA+U 6.0eV
1	+	+	+	+	+	+	+	+	$E0 + 4E1 + 8E2 + 8E3 + 4E4$	0	0
2	+	+	+	+	-	-	-	-	$E0 + 4E1 - 8E2 - 8E3 + 4E4$	-437	-172
3	+	-	-	+	+	+	-	-	$E0 + 4E1 + 4E4$	-218	-88
4	-	-	+	+	+	-	-	+	$E0 - 4E1 - 4E4$	-422	-200
5	+	-	+	-	+	+	-	-	$E0 - 4E1 + 4E4$	-239	-114
6	+	+	+	+	-	+	+	+	$E0 + 4E1 + 4E2 + 4E3$	-171	-87
7	+	-	+	+	-	+	+	+	$E0 + 4E2$	-199	-130
8	+	-	+	+	-	-	+	+	$E0 + 4E2 - 4E3 + 4E4$	-276	-118

From these total energy calculations the exchange integrals were extracted. All were found to be antiferromagnetic in nature within both GGA and GGA+U methods as listed in Table 9. For GGA the third coupling, J_3 , which is the coupling between two NN Fe^{+2} (Fe(1)) and Fe^{+3} (Fe(2)) ions through F(1) ion, is found to be the strongest. The second strongest coupling is J_4 , which accounts for the coupling between two NN Fe^{+3} ions mediated via F(3) ion, is 0.85 of J_3 . However within GGA+U, this J_4 / J_3 ratio gets enhanced with the increase of U and becomes more than 1.0 for $U_{\text{eff}} > 2.0\text{eV}$. The coupling between two NN Fe^{+2} ions, J_1 , and the coupling between two NN Fe^{+2} and Fe^{+3} mediated via F(2) ion, J_2 , remain smaller than J_3 and J_4 (for the whole range of U). These results indicate that the magnetic frustration is partially lifted by the orthorhombic distortion, but not completely, as J_1 and J_2 are not negligible compared to J_3 and J_4 . This residual frustration is therefore a hindrance to achieve a collinear AFM ordering for the system and likely leads to a non-collinear AFM state governed by the strongest exchange integrals.

Table 9. The obtained magnetic exchange integrals in meV and the mean field estimation of Curie-Weiss temperature (Θ_{CW}) in K are listed.

J_i	GGA	GGA+U 6.0 eV
J_1	-1.8	-0.9
J_2	-2.7	-0.7
J_3	-4.0	-1.5
J_4	-3.4	-1.7
Θ_{CW}	-693	-281

Finally we calculated the Curie-Weiss temperature, Θ_{CW} , within mean field theory given by,

$$\Theta_{CW} = \frac{1}{3k_B} (2S_1(S_1 + 1)J_1 + 2S_{12}(S_{12} + 1)(J_2 + J_3) + 2S_2(S_2 + 1)J_4) \quad (2)$$

where S_{12} is the average of S_1 and S_2 . Results are listed in Table 9 where it can be seen that the GGA+U result, $\Theta_{CW} = -281$ K, agrees well with the experimental value of -272 K, extracted from magnetic susceptibility data at high temperatures (Note that this is why we choose to present the U = 6 eV results.)

Conclusion.

We have synthesized and characterized a new charge-ordered magnetically frustrated mixed-metal fluoride, $\text{RbFe}^{2+}\text{Fe}^{3+}\text{F}_6$, that exhibits a pyrochlore-related structure. An anti-ferromagnetic ordering temperature of 16 K was observed, however no structural transition was observed in the variable temperature neutron diffraction data. The theoretical calculations for the Weiss constant resulted in a value of -281 K that agrees well with the experimental value of -272 K. Additional theoretical calculations, neutron diffraction, magnetic, and Mossbauer measurements on RbFe_2F_6 are in progress and will be reported in the near future.

ACKNOWLEDGMENT. Work at UH and Cornell supported by the U.S. Department of Energy, Basic Energy Sciences, Division of Materials Sciences and Engineering under Award # DE-SC0005032. Work at UMN supported by DOE Award #DE-FG02-06ER46275 (magnetic measurements).

Notes and references

^a Department of Chemistry, University of Houston, 136 Fleming Building, Houston, TX 77204-5003, USA: Fax: +011 713-743-0796; Tel: +011 713-743-3278; E-mail: psh@uh.edu

^b Department of Materials Science and Engineering, University of Maryland, College Park, MD, 20742-2115, USA and NIST Center for Neutron Research, National Institute of Standards and Technology, 100 Bureau Drive, Gaithersburg, MD 20899-6103, USA.: Fax: +011 301-975-4297; Tel: +011301-975-4297; E-mail: mark.green@nist.gov

^cDepartment of Chemical Engineering and Materials Science, University of Minnesota, 151 Amundson Hall, 421 Washington Ave. SE,

Minneapolis, MN 55455, USA: Fax: +011 612-624-4578; Tel: +011 612-625-4018; E-mail: Leighton@umn.edu

^dSchool of Applied and Engineering Physics, 271 Clark Hall, Cornell University, Ithaca, NY 14853, USA: Fax: +011 607-255-7658; Tel: +011 607-255-6498; E-mail: fennie@cornell.edu

[†] Electronic Supplementary Information (ESI) available: X-ray crystallographic files in CIF format, experimental and calculated powder X-ray diffraction patterns, Infrared and UV-vis spectra, thermogravimetric and differential thermal analysis diagrams, and additional theoretical calculations. See DOI: 10.1039/b000000x/

- P. Hagenmuller, in *Book Inorganic Solid Fluorides - Chemistry and Physics*, ed., ed. by Editor, Academic Press, City, **1985**.
- M. Eibschutz, H. J. Guggenheim, *Solid State Commun.* 1968, **6**, 737-739.
- M. Eibschutz, H. J. Guggenheim, S. H. Wemple, I. Camlibel, M. DiDomenico, *Phys. Lett.* 1969, **29A**, 409-410.
- E. T. Keve, S. C. Abrahams, J. L. Bernstein, *J. Chem. Phys.* 1969, **51**, 4928-4936.
- E. T. Keve, S. C. Abrahams, J. L. Bernstein, *J. Chem. Phys.* 1970, **53**, 3279-3287.
- J. Ravez, S. Arquis, J. Grannec, *J. Appl. Phys.* 1987, **62**, 4299-4301.
- R. Cosier, A. Wise, A. Tressaud, J. Grannec, R. Olazcuaga, J. Portier, *C. R. Hebd. Seances Acad. Sci. Ser. C* 1970, **271**, 142.
- G. Ferey, R. De Pape, M. Poulain, D. Grandjean, A. Hardy, *Acta Cryst.* 1977, **B33**, 209.
- J. Ravez, S. C. Abrahams, R. De Pape, *J. Appl. Phys.* 1989, **65**, 3987.
- J. Ravez, *J. Phys. III* 1997, **7**, 1129.
- S. C. Abrahams, J. Ravez, A. Simon, J. P. Chaminade, *J. Appl. Phys.* 1981, **57**, 4740-4743.
- J. G. Bergman, G. R. Crane, H. J. Guggenheim, *J. Appl. Phys.* 1975, **46**, 4645-4646.
- K. Shimamura, E. G. Villora, H. Zeng, M. Nakamura, S. Takekawa, K. Kitamura, *Appl. Phys. Lett.* 2006, **89**, 232911-1 - 232911-3.
- R. Blinc, G. Tavcar, B. Zemva, D. Hanzel, P. Cevc, C. Filipic, A. Levstik, Z. Jaglicic, Z. Trontelj, N. Dalal, V. Ramachandran, S. Nellutla, J. F. Scott, *J. Appl. Phys.* 2008, **103**, 074114-1 - 074114-4.
- R. Blinc, G. Tavcar, B. Zemva, E. Goreshnik, D. Hanzel, P. Cevc, A. Potocnik, V. Laguta, Z. Trontelj, Z. Jaglicic, J. F. Scott, *J. Appl. Phys.* 2009, **106**, 023924-1 - 023924-4.
- R. Blinc, P. Cevc, A. Potocnik, B. Zemva, E. Goreshnik, D. Hanzel, A. Gregorovic, Z. Trontelj, Z. Jaglicic, V. Laguta, M. Perovic, N. Dalal, J. F. Scott, *J. Appl. Phys.* 2010, **107**, 043511-1 - 043511-5.
- J. F. Scott, R. Blinc, *J. Phys.: Condens. Matter* 2011, **23**, 1 - 17.
- J. F. Scott, R. Blinc, *J. Phys. Condens. Matter* 2011, **23**, 299401.
- D. Babel, G. Pausewang, W. Viebahn, *Z. Naturforsch.* 1967, **22b**, 1219-1220.
- D. Babel, *Z. Anorg. Allg. Chem.* 1972, **387**, 161-178.
- N. N. Greenwood, A. T. Howe, F. Menil, *J. Chem. Soc. A* 1971, 2218-2224.
- G. Ferey, M. Leblanc, R. De Pape, *J. Solid State Chem.* 1981, **40**, 1-7.
- A. Tressaud, F. Menil, R. Georges, J. Portier, P. Hagenmuller, *Mat. Res. Bull.* 1972, **7**, 1339-1346.
- N. N. Greenwood, F. Menil, A. Tressaud, *J. Solid State Chem.* 1972, **5**, 402-409.
- A.-M. Hardy, A. Hardy, G. Ferey, *Acta Cryst.* 1973, **B29**, 1654-1658.
- R. Masse, J. Leonard, M. T. Averbuch-Pouchot, *J. Solid State Chem.* 1984, **53**, 136.
- J. Gaile, W. Rudorff, W. Viebahn, *Z. Anorg. Allg. Chem.* 1977, **430**, 161.
- S. Roth, W. Kurtz, *Physica* 1977, **86-88B**, 715.

- 29 J. Villain, *Z. Phys. B* 1979, **33**, 31.
- 30 G. Ferey, M. Leblanc, R. de Pape, J. Pannetier, *Solid State Commun.* 1985, **53**, 559-563.
- 31 G. Ferey, M. Leblanc, R. De Pape, *J. Cryst. Growth* 1975, **29**, 209-
5 211.
- 32 E. Herdtweck, *Z. Anorg. Allg. Chem.* 1983, **501**, 131.
- 33 M. Leblanc, G. Ferey, Y. Calage, R. De Pape, *J. Solid State Chem.* 1984, **53**, 360.
- 34 SAINT, Program for Area Detector Absorption Correction, Siemens
10 Analytical X-ray Systems, Inc., Madison, WI, **1995**.
- 35 G. M. Sheldrick, *SHELXS-97 - A program for automatic solution of crystal structures. University of Goettingen: Goettingen, Germany, 1997.*
- 36 G. M. Sheldrick, *SHELXL-97 - A program for Crystal Structure Refinement; University of Goettingen: Goettingen, Germany, 1997.*
- 15 37 L. J. Farrugia, *J. Appl. Crystallogr.* 1999, **32**, 837-838.
- 38 J. Rodriguez-Carvajal, *Phys. B* 1993, **192**, 55.
- 39 P. M. Kubelka, F. Z. Munk, *Tech. Phys.* 1931, **12**, 593.
- 40 J. Tauc, *Mater. Res. Bull.* 1970, **5**, 721-9.
- 41 J. P. Perdew, K. Burke, M. Ernzerhof, *Phys. Rev. Lett.* 1996, **77**,
20 3865.
- 42 P. E. Blöchl, *Phys. Rev. B* 1994, **50**, 17953.
- 43 G. Kresse, J. Hafner, *Phys. Rev. B* 1993, **47**, 558.
- 44 G. Kresse, J. Furthmuller, *Phys. Rev. B* 1996, **54**, 1116.
- 45 V. I. Anisimov, F. Aryasetiawan, A. I. Lichtenstein, *J. Phys.*
25 *Condens. Matter* 1997, **9**, 767.
- 46 S. L. Dudarev, G. A. Botton, S. Y. Savrasov, C. J. Humphreys, A. P. Sutton, *Phys. Rev. B* 1998, **57**, 1505.
- 47 I. D. Brown, D. Altermatt, *Acta Crystallogr., Sect. B* 1985, **B41**, 244-
7.
- 30 48 N. E. Brese, M. O'Keeffe, *Acta Crystallogr., Sect. B* 1991, **B47**, 192-
7.
- 49 K. Nakamoto, *Infrared and Raman Spectra of Inorganic and Coordination Compounds Part A: Theory and Applications in Inorganic Chemistry*. 5th ed., Editor, John Wiley & Sons, Inc., New York, 1997.
- 35 50 M. Leblanc, G. Ferey, Y. Calage, R. de Pape, *J. Solid State Chem.* 1983, **47**, 24-29.
- 51 S. W. Kim, H. Y. Chang, P. S. Halasyamani, *J. Am. Chem. Soc.* 2010, **132**, 17684-17685.
- 52 A. P. Ramirez, *Annu. Rev. Mater. Sci.* 1994, **24**, 453.